XII International Conference on Computational Plasticity. Fundamentals and Applications
COMPLAS XII
E. Oñate, D.R.J. Owen, D. Peric and B. Suárez (Eds)

PULSATILE NON-NEWTONIAN BLOOD FLOW IN IMAGE-BASED MODELS OF CAROTID BIFURCATION

JAN VIMMR*, ALENA JONÁŠOVÁ* AND ONDŘEJ BUBLÍK*

* European Centre of Excellence NTIS – New Technologies for Information Society,
Faculty of Applied Sciences, University of West Bohemia,
Univerzitní 22, CZ-306 14 Pilsen, Czech Republic
e-mail: jvimmr@kme.zcu.cz

Key words: Carotid bifurcation, Non-Newtonian Fluid, Stenosis, Hemodynamics, FVM, Windkessel Model

Abstract. Present hemodynamical study is motivated by the ongoing clinical research at the University Hospital in Pilsen, Czech Republic. On the basis of provided CT scans, several carotid artery models were reconstructed and used for this numerical study of pulsatile blood flow. The blood is modelled as a shear-dependent incompressible fluid, motion of which is described by the non-linear system of Navier-Stokes equations coupled with the Carreau-Yasuda model. The mathematical model is solved using in-house software based on the principle of the SIMPLE algorithm and cell-centred finite volume method (FVM) formulated for hybrid unstructured tetrahedral grids. The discussion of obtained numerical results is performed with special emphasis placed on the analysis of velocity field and distribution of main hemodynamic factors such as cycle-averaged WSS and oscillatory shear index (OSI) in areas prone to atherosclerosis.

1 INTRODUCTION

Besides the coronary heart disease, the stroke is a prevalent and severe medical condition that imposes an immense loss of health and heavy economic burden in many European countries[8]. One of the most frequently involved sites in the large artery atherothrombotic stroke is the carotid bifurcation[11], particularly the origin of the internal carotid artery with a unique vessel expansion, commonly known as the carotid sinus. In the past several studies[4, 5] have indicated that vessel morphology and accompanying hemodynamics play a key role in the localisation of atherosclerotic plaque and in its vulnerability to rupture or erosion. In later studies, especially those presenting results of numerical simulations[12, 13, 14], the correlation between the hemodynamics and atherogenesis has been confirmed and led to further numerical and experimental investigations. According to several recent works[3, 6, 7], there are many indicators of disturbed blood flow such as helical flow that may help in the localisation of sites prone to atherothrombotic carotid stenosis formation.

This preliminary hemodynamical study, motivated by our co-operation with the University Hospital in Pilsen, is focused on numerical modelling of pulsatile blood flow in patient-specific models of the left and right carotid arteries in various advanced stages of atherosclerosis. In contrast to other studies[3, 13], we implement our own computational software, which has been developed and successfully implemented for the modelling of non-Newtonian hemodynamics in realistic models of various aorto-coronary bypasses[10]. For the carotid artery models applied in this study, we consider the complex rheological properties of human blood and prescribe physiological boundary conditions corresponding to those usually found in the carotid arteries. The obtained results are analysed with emphasis placed on the distribution of velocity and the presence of low and oscillatory wall shear stress[4] in the vicinity of the stenosed carotid bifurcation.

2 CAROTID MODELS AND MODELLING ASSUMPTIONS

For the modelling of non-Newtonian blood flow in realistic carotid geometries, three different sets of medical data were provided by the University Hospital in Pilsen, Czech Republic. The obtained CT scans were of three older patients (2 female and 1 male) with different stages of atherosclerotic plaque formation in the region of carotid bifurcation, see the atherosclerotic calcifications in red shown in Fig. 2. For the primary reconstruction process, we employed the semi-automatic segmentation in-house software DICOM2FEM (`https://github.com/vlukes/dicom2fem`) developed at the University of West Bohemia in Czech Republic. With the well-known Taubin smoothing algorithm[9], the coarse surface mesh of each carotid model was smoothed and consequently remeshed using the software package HyperMesh v11.0 (Altair Engineering, Troy, USA), Fig. 1.

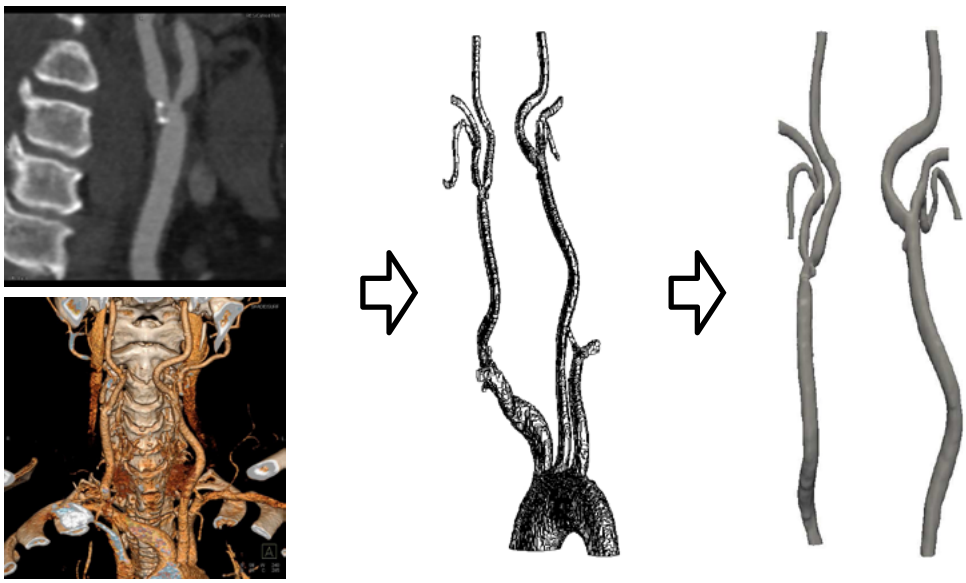

Figure 1: Raw model reconstructed from CT scans and final carotid model after smoothing

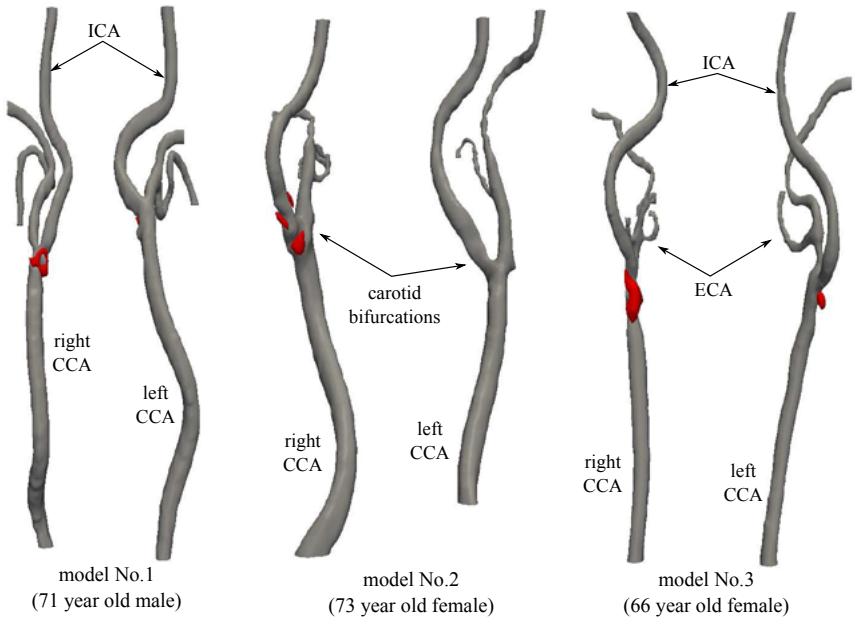

Figure 2: Three patient-specific carotid models with atherosclerotic calcifications in red (CCA = common carotid artery, ICA = internal carotid artery, ECA = external carotid artery)

Human blood as a suspension of cellular elements in pale-yellow plasma is known to exhibit complex rheological behaviour that can be characterised by shear-dependent viscosity and viscoelasticity. In vessels with inner diameters greater than 1 mm[2], the non-Newtonian viscosity becomes the main factor that determines the flow properties of the whole blood. Thus, in this study we consider human blood to be an incompressible generalised Newtonian fluid with constant density $\varrho = 1050\,\mathrm{kg\,m^{-3}}$ and shear-dependent dynamic viscosity given by a suitable constitutive model. Assuming laminar flow throughout the entire cardiac cycle, all numerical simulations of pulsatile blood flow are carried out for carotid models with impermeable and non-compliant walls. Note that this modelling approach is also motivated by other studies[3, 6, 7], where similar assumptions are taken into account.

3 MATHEMATICAL MODELLING

3.1 Mathematical model

Let us consider a time interval $(0, \mathcal{T})$, $\mathcal{T} > 0$ and a bounded three-dimensional computational domain $\Omega \subset \mathbf{R}^3$ with boundary $\partial\Omega = \partial\Omega_I \cup \partial\Omega_O \cup \partial\Omega_W$, where $\partial\Omega_I$, $\partial\Omega_O$ and $\partial\Omega_W$ denote the inlet, outlet and walls of the computational domain, respectively. Let us further assume that the blood flow in the carotid arteries is unsteady, laminar and isothermal. Then in the space-time cylinder $\Omega_T = \Omega \times (0, \mathcal{T})$, the motion of blood can be mathematically described by the non-linear system of Navier-Stokes (NS) equations for

an incompressible generalised Newtonian fluid as follows:

$$\frac{\partial v_i}{\partial x_i} = 0\,, \tag{1}$$

$$\frac{\partial v_i}{\partial t} + \frac{\partial}{\partial x_j}(v_i v_j) + \frac{1}{\varrho}\frac{\partial p}{\partial x_i} = \frac{1}{\varrho}\frac{\partial}{\partial x_j}\left[\eta(\dot\gamma)\,\left(\frac{\partial v_i}{\partial x_j} + \frac{\partial v_j}{\partial x_i}\right)\right], \quad i,j = 1,2,3\,, \tag{2}$$

where v_i is the ith component of the velocity vector $\boldsymbol{v} = [v_1, v_2, v_3]^T$ corresponding to the Cartesian component x_i of the space variables vector $\boldsymbol{x} = [x_1, x_2, x_3]^T \in \Omega$, $t \in (0, \mathcal{T})$ is the time, p is the pressure, and ϱ is the density of the fluid.

For the modelling of blood' non-Newtonian behaviour, the system of NS equations (1) and (2) is coupled with the Carreau-Yasuda model for the dynamic viscosity $\eta(\dot\gamma)$

$$\eta(\dot\gamma) = \eta_\infty + (\eta_0 - \eta_\infty)\Big[1 + \big(\lambda\dot\gamma\big)^a\Big]^{\frac{n-1}{a}}. \tag{3}$$

In accordance with our previous work[10], the Carreau-Yasuda model employs following parameters[2]: $\eta_0 = 56 \times 10^{-3}\,\mathrm{Pa\,s}$, $\eta_\infty = 3.45 \times 10^{-3}\,\mathrm{Pa\,s}$, $\lambda = 1.902\,\mathrm{s}$, $a = 1.25$ and $n = 0.22$. The shear rate $\dot\gamma$ appearing in Eq. (3) can be computed from $\dot\gamma = 2\sqrt{D_{II}}$, where D_{II} is the second invariant of the deformation rate tensor $\mathbf{D} = \frac{1}{2}\left(\nabla\boldsymbol{v} + (\nabla\boldsymbol{v})^T\right)$. Assuming the blood to be an incompressible fluid, the second invariant simplifies to $D_{II} = \frac{1}{2}\,d_{ij}d_{ij}$, $i,j = 1,2,3$, where d_{ij} are the components of the deformation rate tensor $\mathbf{D}$.

For the three different carotid models described above, the numerical simulations of the pulsatile non-Newtonian blood flow are carried out with following boundary values:

- *Inlet* $\partial\Omega_I$: constant time-dependent velocity profile $|\boldsymbol{v}_I|$ given by the velocity waveform for the common carotid artery shown in Fig. 3 (left), where one period of the cardiac cycle T is approximately 0.81 s.
- *Outlets* $\partial\Omega_O$: 3-element Windkessel model (WM), Fig. 3 (right),

$$\frac{\mathrm{d}p_O}{\mathrm{d}t} + \frac{1}{CR_d}p_O = R_p\frac{\mathrm{d}Q_O}{\mathrm{d}t} + \frac{R_p + R_d}{CR_d}Q_O\,, \tag{4}$$

  where Q_O and p_O are the flow rate and pressure computed at $\partial\Omega_O$ of the 3D carotid model, C, R_p and R_d are the capacitance, proximal and distal resistances of the 3-element WM, respectively. For the parameters of the WM at each carotid outlet, see Table 1.
- *Impermeable and non-compliant walls* $\partial\Omega_W$: non-slip boundary condition $\boldsymbol{v} = \mathbf{0}$.

3.2 Numerical method

The numerical solution of the mathematical model, which is given by the non-linear time-dependent system of NS Eqs (1)–(2) coupled with the Carreau-Yasuda model (3), is based on the principle of the SIMPLE algorithm and the cell-centred finite volume method

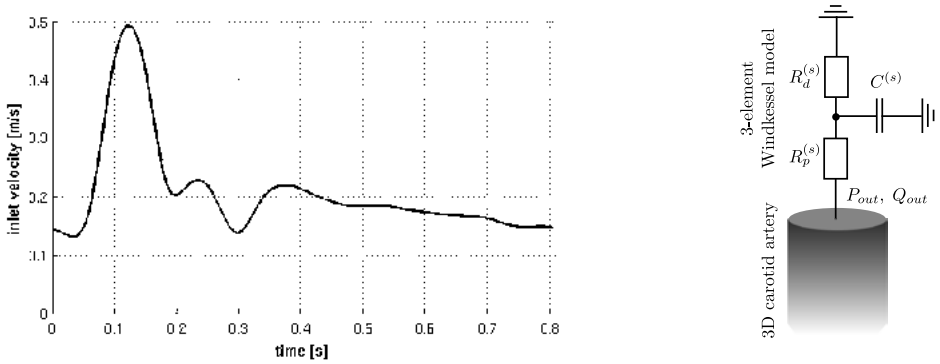

Figure 3: Velocity waveform in the common carotid artery[14] (left). Schematic drawing of the 3-element Windkessel model prescribed as an outlet boundary condition (right).

Table 1: Parameters of the 3-element Windkessel model. Here the index s denotes the outlet number corresponding to one of the three carotid models

		s	area $A\,[\mathrm{cm}^2]$	$R_p^{(s)} \times 10^6$ $[\mathrm{Pa\,s/m}^3]$	$R_d^{(s)} \times 10^6$ $[\mathrm{Pa\,s/m}^3]$	$C^{(s)} \times 10^{-10}$ $[\mathrm{m}^3/\mathrm{Pa}]$
model No.1	left	1	0.228	241.4	2429.1	7.40
		2	0.070	786.3	7912.0	2.27
		3	0.176	312.7	3148.7	5.71
	right	1	0.166	331.6	3336.9	5.39
		2	0.051	1079.2	10859.6	1.66
		3	0.155	355.1	3573.2	5.03
model No.2	left	1	0.139	396.0	3984.5	4.51
		2	0.023	2393.0	24080.0	0.75
		3	0.063	873.6	8791.1	2.04
	right	1	0.138	398.8	4013.3	4.48
		2	0.010	5504.0	55384.0	0.32
		3	0.011	5003.6	50349.1	0.36
		4	0.019	C13	C12	C13
model No.3	left	1	0.036	1528.9	15384.4	1.17
		2	0.022	2501.8	25174.5	0.71
		3	0.086	640.0	6440.0	2.79
	right	1	0.110	500.4	5034.9	3.57
		2	0.014	3931.4	39560.0	0.45
		3	0.020	2752.0	27692.0	0.65
		4	0.007	7862.9	79120.0	0.23
		5	0.029	1897.9	19097.9	0.94

formulated for hybrid unstructured tetrahedral grids. Because the whole computational algorithm is described in more detail in one of our previous studies[10], only the basic relationships will be mentioned here.

Let Ω_k, $k = 1, 2, \ldots, N_{CV}$ be the control volume of the tetrahedral computational mesh with values of pressure $(p)_k$ and Cartesian velocity components $(v_i)_k$, $i = 1, 2, 3$ defined in the centre of each control volume Ω_k as an integral average. In addition to those variables, the hybrid mesh approach requires the face-normal velocity $V_m = v_{im} \cdot {}^i n_k^m$, $m = 1, \ldots, 4$, which has the direction of the outward unit vector $\boldsymbol{n}_k^m$ normal to the mth face Γ_k^m of the control volume Ω_k. For the computational algorithm, we introduce an intermediate velocity $(\hat{v}_i)_k$ and a pressure correction function in the form $(\Psi)_k = \frac{2}{3}\Delta t[(p^{n+1})_k - (p^n)_k]$, where $(p^{n+1})_k$ and $(p^n)_k$ are the values of pressure computed at the time levels n and $(n+1)$, respectively.

After time integration with an implicit multistep method of second order accuracy and spatial discretisation using the cell-centred finite volume method, the system of Eqs (1)–(2) leads to the following form:

$$\frac{3}{2\Delta t}(\hat{v}_i)_k - \frac{2}{\Delta t}(v_i^n)_k + \frac{1}{2\Delta t}(v_i^{n-1})_k + \frac{1}{|\Omega_k|}\sum_{m=1}^{4} \hat{v}_{im}|_{\text{upwind}}\, V_m^s\, |\Gamma_k^m| +$$

$$+\frac{1}{\varrho|\Omega_k|}\sum_{m=1}^{4} p_m^s \cdot {}^i n_k^m\, |\Gamma_k^m| = \frac{1}{\varrho|\Omega_k|}\sum_{m=1}^{4} \eta(\dot{\gamma}(v^n))^m \left(\frac{\partial \hat{v}_i}{\partial x_j}\bigg|_{\Gamma_k^m} + \frac{\partial v_j^s}{\partial x_i}\bigg|_{\Gamma_k^m} \right) \cdot {}^j n_k^m\, |\Gamma_k^m|, \qquad (5)$$

$$\frac{1}{\varrho}\sum_{m=1}^{4} \frac{\partial \Psi}{\partial \boldsymbol{n}_k^m}|\Gamma_k^m| = \sum_{m=1}^{4} \hat{v}_{im} \cdot {}^i n_k^m |\Gamma_k^m| \equiv \sum_{m=1}^{4} \hat{V}_m |\Gamma_k^m|, \qquad (6)$$

$$(v_i^{s+1})_k = (\hat{v}_i)_k - \frac{1}{\varrho|\Omega_k|}\sum_{m=1}^{4} \Psi_m \cdot {}^i n_k^m |\Gamma_k^m|, \qquad (7)$$

$$(p^{s+1})_k = (p^s)_k + \alpha \frac{3}{2\Delta t}(\Psi)_k, \qquad (8)$$

$$V_m^{s+1} = \hat{V}_m - \frac{1}{\varrho}\frac{\partial \Psi}{\partial \boldsymbol{n}_k^m}, \qquad (9)$$

where $(v_i^n)_k$ and $(v_i^{n-1})_k$ are the velocities computed at the time levels n and $(n-1)$, respectively, $\Delta t = t^{n+1} - t^n$ is the time step, $|\Omega_k|$ is the volume of the tetrahedral control volume Ω_k, ${}^i n_k^m$ is the ith component of the outward unit vector $\boldsymbol{n}_k^m = [{}^1 n_k^m, {}^2 n_k^m, {}^3 n_k^m]^T$ normal to the mth face Γ_k^m of the control volume Ω_k, $|\Gamma_k^m|$ denotes the area of the mth face Γ_k^m of the control volume Ω_k, $\alpha \in (0, 1]$ is an under relaxation parameter and $\hat{V}_m = \hat{v}_{im} \cdot {}^i n_k^m$ is the intermediate face-normal velocity at the mth face Γ_k^m of the control volume Ω_k. In Eqs (5)–(9), we introduced the inner iteration index s as $(v_i^{s=0})_k = (v_i^n)_k$ and $(p^{s=0})_k = (p^n)_k$. The computation is repeated for $s = 0, 1, 2, 3, \ldots$ so long until $(\Psi)_k$ does not satisfy

a convergence criterion $\frac{1}{N_{CV}}\|\boldsymbol{\Psi}\|_{l_2} < 10^{-2}$. At the end of the inner iteration process, we set $(v_i^{n+1})_k = (v_i^{s+1})_k$ and $(p^{n+1})_k = (p^{s+1})_k$.

The values p_m^s, $\hat{v}_{im}$, Ψ_m, and the derivatives $\frac{\partial \Psi}{\partial \boldsymbol{n}_k^m}$, $\left.\frac{\partial \hat{v}_i}{\partial x_j}\right|_{\Gamma_k^m}$, $\left.\frac{\partial v_j^s}{\partial x_i}\right|_{\Gamma_k^m}$ at the mth face Γ_k^m of the control volume Ω_k are determined using an appropriate interpolation method[10]. In accordance with the numerical method described above, following types of boundary conditions are prescribed:

- inlet $\Gamma_k^m \subset \partial\Omega_I$: $\hat{v}_{im} = v_{iI}$, $\left.\frac{\partial \hat{v}_i}{\partial x_j}\right|_{\Gamma_k^m} = 0$, $\left.\frac{\partial \Psi}{\partial \boldsymbol{n}_k^m}\right|_{\Gamma_k^m} = 0$, where the inlet velocity vector components $v_{i\,I}$ are given according to the velocity waveform shown in Fig. 3 (left);
- outlet $\Gamma_k^m \subset \partial\Omega_O$: $p_m = p_O$, $\left.\frac{\partial \hat{v}_i}{\partial x_j}\right|_{\Gamma_k^m} = 0$, $\Psi_m = 0$, where p_O is the value of outlet pressure computed with the help of the discretised form of Eq. (4);
- non-compliant and impermeable wall $\Gamma_k^m \subset \partial\Omega_W$: $\hat{v}_{im} = 0$, $\left.\frac{\partial \Psi}{\partial \boldsymbol{n}_k^m}\right|_{\Gamma_k^m} = 0$.

The solution of Eq. (5) leads to a system of linear algebraic equations $\mathbf{A}_{NS} \cdot \mathbf{x}_{NS} = \mathbf{b}_{NS}$ for $3\,N_{CV}$ unknown values $(\hat{v}_i)_k$, $i = 1, 2, 3$, $k = 1, 2, \ldots N_{CV}$, where N_{CV} is the number of control volumes constituting the hybrid unstructured computational mesh. The solution of the Poisson Eq. (6) for the pressure correction function leads to a system of linear algebraic equations $\mathbf{A}_{Poi} \cdot \mathbf{x}_{Poi} = \mathbf{b}_{Poi}$ for N_{CV} unknown values $(\Psi)_k$, $k = 1, 2, \ldots N_{CV}$. Because of the large sparse matrices $\mathbf{A}_{NS}$ and $\mathbf{A}_{Poi}$, the systems of equations are solved iteratively using the BICGSTAB method with incomplete LU preconditioner implemented in the MATLAB software.

4 NUMERICAL RESULTS

On the basis of the numerical method described above, numerical computations were carried out with selected results that will be discussed in the remainder of this section.

Figs 4–5 show the velocity distribution in two of the three reconstructed carotid artery models (No.2 and No.3). To better represent the complex 3D blood flow observed in the two models, the obtained flow fields are shown in the form of streamlines coloured by the velocity magnitude $|\boldsymbol{v}|$ [m/s] at four selected time instants of the cardiac cycle ($t_1 = 0.03\,\mathrm{s}$, $t_2 = 0.15\,\mathrm{s}$, $t_3 = 0.25\,\mathrm{s}$, $t_3 = 0.60\,\mathrm{s}$). From both figures, it becomes quite apparent that a large portion of blood passing through the common carotid artery (CCA) is directed toward the internal carotid artery (ICA). This observation is in accordance with other studies[6], where similar flow division was noted. Regardless of the phase of the cardiac cycle, all of the carotid artery models are characterised by a strongly disturbed flow field in the bifurcation region and in the external carotid artery (ECA). In this case, it is possible to point out the presence of several large- and small-sized recirculation zones, see, for example, the entrance of the ECA in Fig. 4a-b or the first part of the ICA in Fig. 5d.

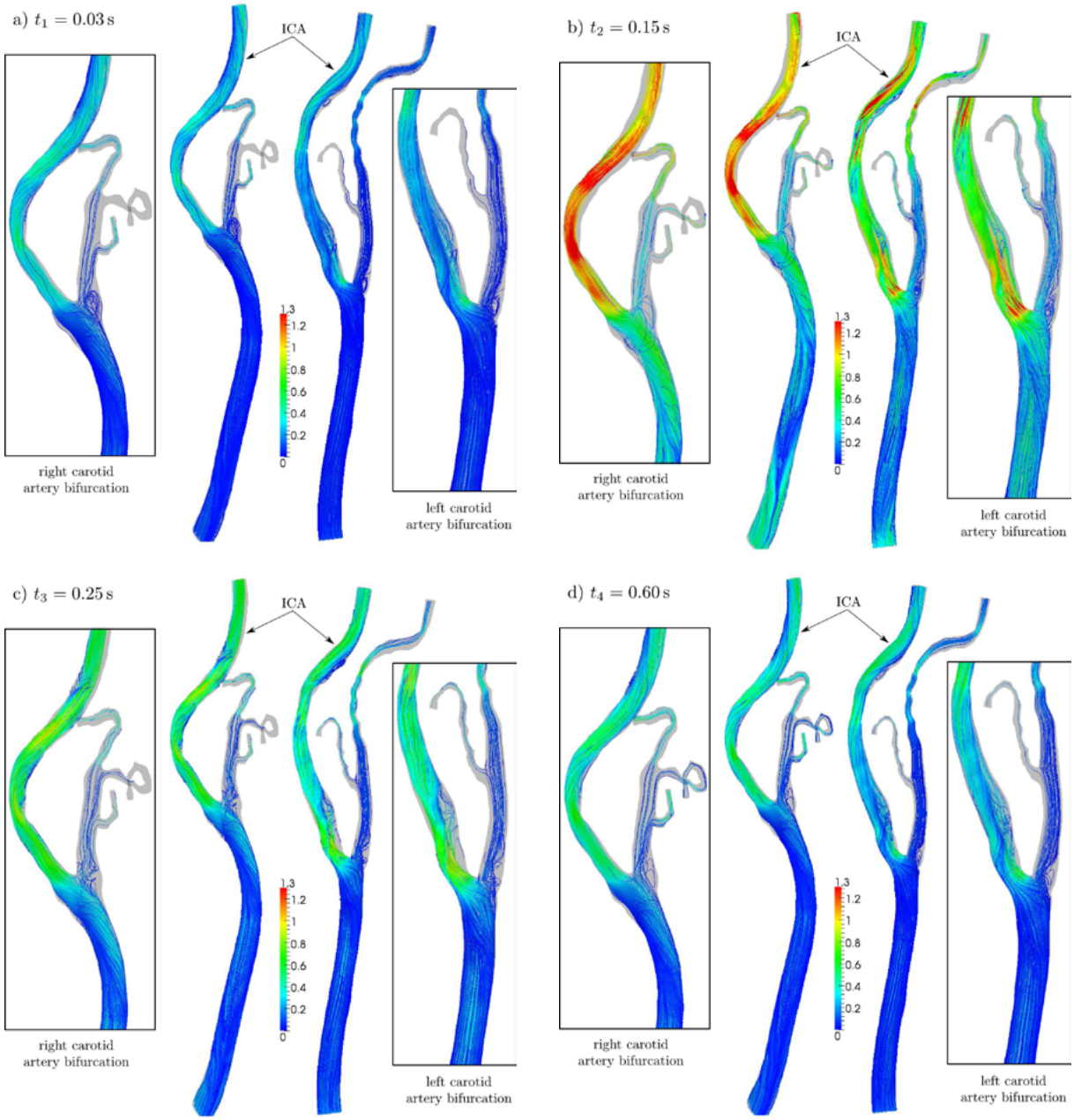

Figure 4: Carotid artery model No.2 – streamlines at four selected time instants ($|\boldsymbol{v}|$ [m/s])

In addition to disturbed flow field, the growth of an atherosclerotic plaque in carotid arteries is also known to be triggered and stimulated by the presence of low and oscillatory wall shear stress[4]. Fig. 6 shows the distributions of the cycle-averaged wall shear stress (WSS) and oscillatory shear index (OSI) in the two models discussed above. Because low values of WSS are of main interest here, the WSS distribution in Fig. 6(top) is

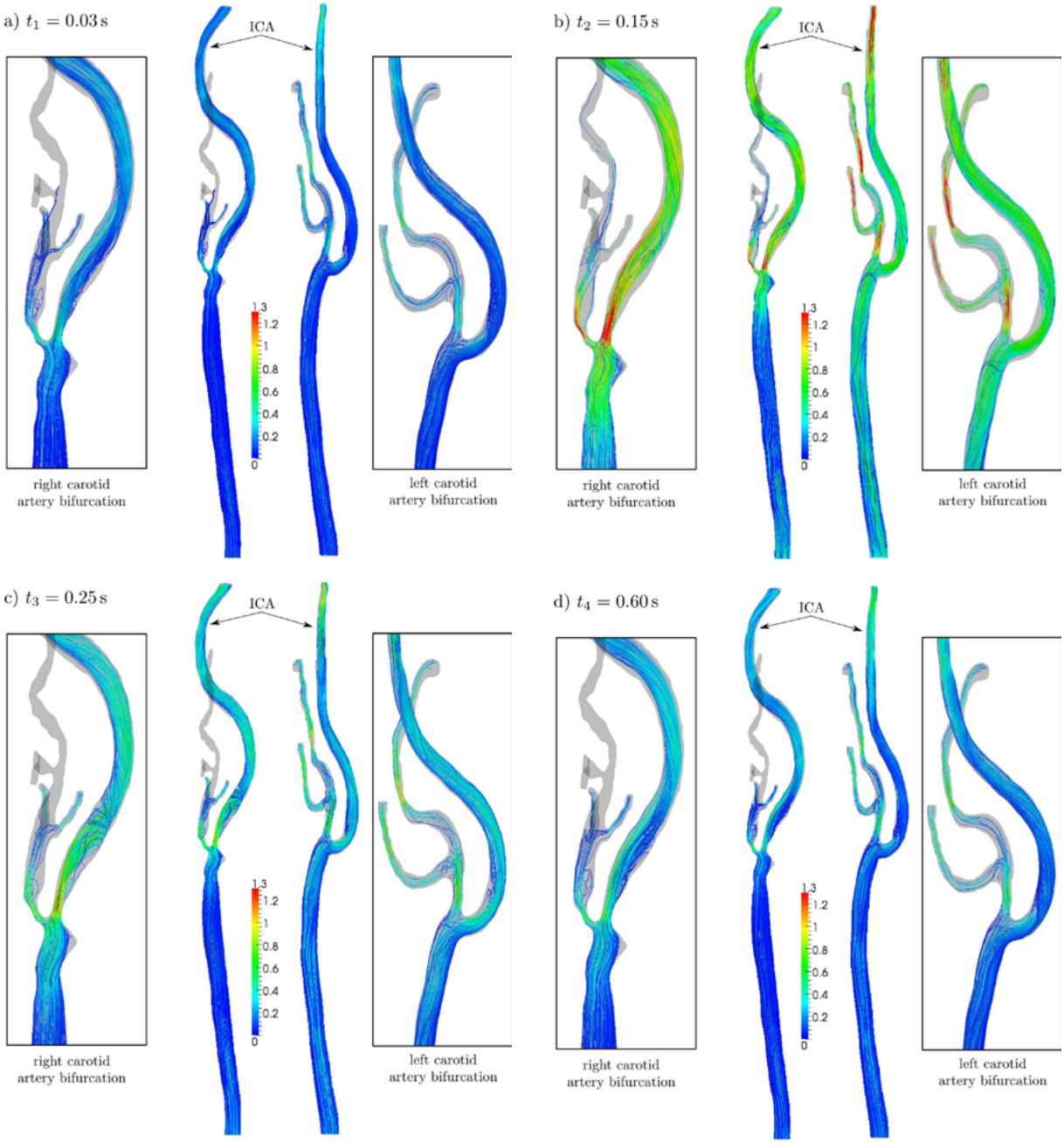

Figure 5: Carotid artery model No.3 – streamlines at four selected time instants ($|\boldsymbol{v}|$ [m/s])

shown with a lowered value range from 1 to 4 Pa. Overall, the shear results indicate a tendency to inadequate shear stimulation (WSS < 1 Pa) in regions occupied by stagnant flow or recirculation zones. In the case of the carotid artery model No.2, Fig. 6 (top), this correlation is particularly noticeable by the left ECA, where a low WSS area near the

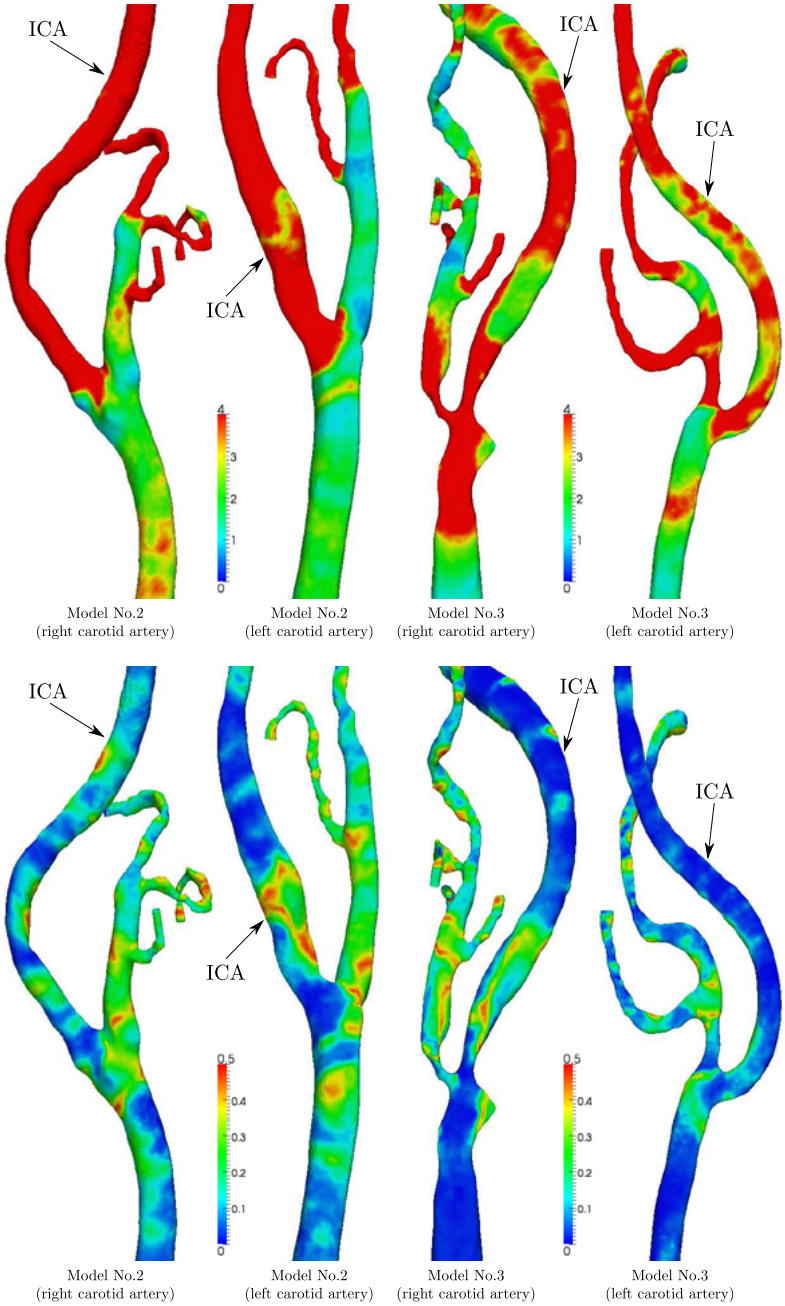

Figure 6: Distribution of cycle-averaged WSS [Pa] (up) and OSI [–] (bottom) in the two selected models of the carotid artery

bifurcation is the result of flow disturbances and recirculation, see Fig. 4. Besides low shear values, the non-uniform hemodynamics in the vicinity of stenosed carotid bifurcations also shows a tendency to strong shear oscillation, Fig. 6(bottom). Particularly affected are, in this case, the downstream regions of both the ICA and ECA, where the OSI exceeds 0.4.

5 CONCLUSIONS

This preliminary hemodynamical study was focused on the numerical simulation of pulsatile non-Newtonian blood flow in the three different carotid artery models reconstructed from CT scans. All of the obtained numerical results showed that the shape and size of the atherosclerotic plaque in the vicinity of the carotid bifurcation significantly affects the resulting flow field and the distribution of hemodynamical wall parameters (WSS and OSI). Overall, the character of the blood flow tended towards non-uniformity with several stagnation and recirculation zones in the first parts of the ICA and ECA.

In the near future, we are going to deepen our co-operation with the University Hospital in Pilsen by further developing our present computational software. One of the possibilities for improvement may be seen in the consideration of some mathematical models describing the growth of an atherosclerotic plaque in relevant sites of the carotid bifurcation[1] or in the modelling of not so common problems such as the interaction between the pulsatile blood flow and a loosened thrombus (embolus) in the bloodstream of the carotid artery.

ACKNOWLEDGMENT

This study was supported by the European Regional Development Fund (ERDF), project "NTIS - New Technologies for Information Society", European Centre of Excellence, CZ.1.05/1.1.00/02.0090.

REFERENCES

[1] Calvez, V., Ebde, A., Meunier, N. and Raolut, A. Mathematical modelling of the atherosclerotic plaque formation. *Esaim: Proceedings* (2009) **28**:1-12.

[2] Cho, Y.I. and Kensey, K.R. Effects of the non-Newtonian viscosity of blood on flows in diseased arterial vessels – part I: Steady flows. *Biorheology* (1991) **28**: 241–262.

[3] Gallo, D., Steinman, D.A., Bijari, P.B. and Morbiducci, U. Helical flow in carotid bifurcation as surrogate marker of exposure to disturbed shear. *J. Biomech.* (2012) **45**:2398–2404.

[4] Ku, D.N., Giddens, D.P., Zarins, C.K. and Glagov, S. Pulsatile flow and atherosclerosis in the human carotid bifurcation – Positive correlation between plaque location and low and oscillating shear stress. *Arterioscler. Thromb. Vasc. Biol.* (1985) **5**:293–302.

[5] Malek, A.M., Alper, S.L. and Izumo, S. Hemodynamic shear stress and its role in atherosclerosis. *JAMA – J. Am. Med. Assoc.* (1999) **282**:2035–2042.

[6] Massai, D., Soloperto, G., Gallo, D., Xu, X.Y. and Morbiducci, U. Shear-induced platelet activation and its relationship with blood flow topology in a numerical model of stenosed carotid bifurcation. *Eur. J. Mech. B-Fluid.* (2012) **35**:92–101.

[7] Morbiducci, U., Gallo, D., Massai, D., Ponzini, R., Deriu, M.A., Antiga, L., Redaelli, A. and Montevecchi, F.M. On the importance of blood rheology for bulk flow in hemodynamic models of the carotid bifurcation. *J. Biomech.* (2011) **44**:2427–2438.

[8] Nichols, M., Townsend, N., Scarborough, P. and Rayner, M. *European cardiovascular disease statistics 2012 edition*. European Heart Network, (2012).

[9] Taubin, G. A signal processing approach to fair surface design. In: *Proceedings of the 22nd annual conference on Computer graphics and interactive techniques – ACM SIGGRAPH 95*, New York, (1995), pp. 351-358.

[10] Vimmr, J., Jonášová, A. and Bublík, A. Numerical analysis of non-Newtonian blood flow and wall shear stress in realistic single, double and triple aorto-coronary bypasses. *Int. J. Numer. Meth. Bio.* (2013), doi: 10.1002/cnm.2560 (accepted for publication).

[11] Wakhloo, A.K., Lieber, B.B., Seong, J., Sadasivan, C., Gounis, M.J., Miskolczi, L. and Sandhu, J.S. Hemodynamics of carotid artery atherosclerotic occlusive disease. *J. Vasc. Interv. Radiol.* (2004) **15**:S111-S121.

[12] Younis, H.F., Kaasempur-Mofrad, M.R., Chan, R.C., Isasi, A.G., Hinton, D.P., Chau, A.H., Kim, L.A. and Kamm, R.D. Hemodynamics and wall mechanics in human carotid bifurcation and its consequences for atherogenesis: Investigation of inter-individual variation. *Biomech. Model. Mechanobiol.* (2004) **3**:17–32.

[13] Younis, H.F., Spring, S., Neumann, S.O and Weigand, B. Simulation of flow in an exact replica of a diseased human carotid artery. *Appl. Math. Model.* (2007) **31**:2599–2609.

[14] Zhao, S.Z., Ariff, B., Long, Q., Hughes, A.D., Thom,S.A., Stanton, A.V., Xua, X.Y. Inter-individual variations in wall shear stress and mechanical stress distributions at the carotid artery bifurcation of healthy humans. *J. Biomech.* (2002) **35**:1367–1377.